The anti-cyclonic gyre around the Qingdao cold water mass in the China marginal sea.

5 Lin Lin[1, a,*] , Hans von Storch[1], Yang Ding[2]

[1]Institute of Coastal Systems, Helmholtz Zentrum Hereon, Geesthacht, 21502, Germany
[2]Frontier Science Center for Deep Ocean Multispheres and Earth System (FDOMES) and Physical Oceanography Laboratory, Ocean University of China, Qingdao, 266100, China
10 [a]Currently at Max Planck Institute for Meteorology, Hamburg, 20146, Germany

Correspondence to: Lin Lin (lin.lin@mpimet.mpg.de).

Abstract. The circulation structure surrounding the Qingdao cold water mass in 2019 was investigated via three-
15 dimensional numerical simulations. The study reveals that a cold pool appears in early spring and reaches its peak in late May, and this pool is accompanied by a local anticyclonic gyre. Momentum diagnostics are utilized to determine the relationship between the cold pool and this gyre. The momentum results reveal that vertical friction cannot be ignored due to the shallow topography and surface wind stress; as a result, the geostrophic balance is no longer applicable in the Qingdao cold water mass region. Consequently, the temperature and salinity gradients induced by the cold pool structure do not
20 directly result in the anticyclonic gyre. Additional numerical experiments are conducted in which tidal forcing or wind forcing is excluded to understand the formation mechanism of this anticyclonic gyre. The t test results show that the difference between the control run and the ensemble experiments without tidal forcing (or without wind forcing) is statistically significant. Thus, both tidal forcing and wind forcing have a significant influence on the anticyclonic structure, although their impacts are different. Without tidal forcing, an unrealistic strong current appears throughout the domain.
25 Moreover, the direction of the eastern side of the anticyclonic circulation is reversed. On the other hand, the wind forcing contributes to the magnitude of the anticyclonic circulation, especially in the western portion of the anticyclonic circulation. Additionally, subcirculation occurs vertically around the Qingdao cold water mass and is influenced by both wind and tidal forcings.

30

1. Introduction

The Qingdao cold water mass was first identified in 1959 and occurs in deep waters below 25 m in the southeastern offshore region of Qingdao during the spring season (The position of Qingdao is shown in Fig. 1) (Ho et al., 1959). This cold water mass is an isolated cold pool characterized by low temperature (6.5-10.0°C), moderate salinity (31.5-32.5), and seasonal variation (Zheng & Zhang, 1983). This cold water mass exerts a significant influence on aquaculture in China since it is situated near the Chinese coastline (Cunyi Zhang, 1986; Y. Zhang & Geng, 1989; Zheng & Zhang, 1983); the temperature, salinity, and circulation distribution of the Qingdao cold water mass play important roles in the ecosystem, such as in primary production (Q. Wei et al., 2019). Numerous researchers have conducted surveys on the origin and characteristics of the Qingdao cold water mass and found that it forms in late April, reaches its peak in May, and gradually moves eastward, with both temperature and salinity increasing. After June, this cold water mass gradually disappears with its emergence in the bottom layer of the Yellow Sea (Diao, 2015; Yu et al., 2006; Q. Zhang et al., 1994, 2004).

Although the Qingdao cold water mass lifetime is relatively short, it is considered an independent water mass because of its unique patterns of both formation and evolution. Based on observational data, Zhang et al. (2002) analyzed the source and temperature-salinity characteristics of the Qingdao cold water mass, indicating that it formed in the local environment by the Bohai Sea coastal current bypassing the Shandong Peninsula. This cold water mass exhibits characteristics of low temperature, low salinity, and high dissolved oxygen. Zhang et al. (2004) analyzed the intensity variations in the Qingdao cold water mass, and their results suggest that it forms from March to April, reaches its peak in May, and disappears gradually in June and July. However, some research cruises observed the presence of the Qingdao cold water mass in August (J. Xia & Xiong, 2013). Yu et al. (2005, 2006) analyzed the relationship between the Qingdao cold water mass and the Yellow Sea cold water mass and reported that in June, the Qingdao cold water mass was already on the edge of the Yellow Sea cold water mass; it was no longer a local independent water mass but rather a local cold center within the Yellow Sea cold water mass. Huang et al. (2019) used numerical simulations to reveal that the cold and low-salinity water in the offshore area between Qingdao and Shidao in the southwestern Yellow Sea was an early form of the Qingdao cold water mass (The position of Shidao is shown in Fig. 1). Additionally, the strong temperature gradient is the thermodynamic mechanism by which the Qingdao cold water mass forms. Based on previous research, conclusions have been drawn regarding the seasonal variations and origins of the Yellow Sea cold water mass. Previous work demonstrated that a mesoscale anticyclone exists near the Qingdao coast, and its position is close to the Qingdao cold water mass (Huang et al., 2019; F. Zhang et al., 1987).

There are other cold water masses in the Bohai and Yellow Seas, the marginal seas along China, such as the cold pool in the Bohai Sea (Liu et al., 2003; Wan et al., 2004; Zhou et al., 2017) and the Yellow Sea cold water mass (Ho et al., 1959; Hur et al., 2000; H. Wei et al., 2010; Yuan et al., 2013). There are usually special circulation structures around cold water masses (C. Xia et al., 2006; Zhou et al., 2017). For example, the Yellow Sea cold water mass, which is a remarkable phenomenon in the Yellow Sea, exists in the bottom layer under the stratification that exists in the center of the Yellow Sea (Wang et al., 2014; Zhu & Wu, 2018). The Yellow Sea cold water mass shows obvious seasonality, starting in spring, peaking in summer,

65   and then decreasing gradually in autumn. Xia et al. (2006) suggested the presence of a Yellow Sea basin-scale anticlockwise gyre at a depth of 4-40 m. This anticlockwise structure is mainly composed of quasigeostrophic flow along the tidal-induced temperature front, and it is strengthened by the tidal residual current based on the momentum balance. The circulation structure around the Yellow Sea cold water mass is apparent, but the anticyclone current field analysis near the Qingdao cold water mass still needs to be investigated. The following questions need to be answered, for example, whether the

70   quasigeostrophic balance is accomplished in the anticyclone area.

In this paper, we investigate the following questions: (1) Is the Qingdao cold water mass, a special cold pool structure, the cause of the local anticyclonic structure? Does such an anticyclonic gyre fit the geostrophic balance? (2) What factors influence the anti-cyclonic gyre horizontally and vertically?

The paper is organized as follows. The model configuration and model design are described in section 2. Section 3 shows the

75   results regarding the simulated temperature, salinity, circulation structures, and momentum balance in the Qingdao cold water mass. In section 4, potential factors affecting the horizontal circulation pattern and the upwelling structures of the Qingdao cold water mass are discussed. Finally, conclusions are given in section 5.

2. Methods and model

80   ### 2.1 Model configuration

In this paper, we use the three-dimensional unstructured grid finite volume coastal ocean model (FVCOM) (Chen & Cowles, 2006). The horizontal grid resolution is approximately 4 km in the Bohai and 8 km in the Yellow Sea, while vertically, the model consists of 30 sigma layers. The vertical and horizontal diffusion coefficients are calculated by the Mellor and Yamada level 2.5 (MY-2.5) turbulent closure model (Mellor & Yamada, 1982) and the Smagorinsky eddy parameterization

85   method, respectively. The model domain includes the Bohai and Yellow Sea, ranging from 31.885°N to 40.942°N and from 117.572°E to 126.915°E, respectively (Fig. 1 in Lin et al. (2023)). The open boundary across the Yellow Sea extends from Qidong in China eastward to the southern tip of the Korean Peninsula, and radiation boundary conditions are used. For the control run, the six-hourly surface forcing data utilized in this study are from the National Centers for Environmental Prediction (NCEP) Climate Forecast System Version 2 (CFSv2) data, featuring a global resolution of 0.2°×0.2°. This dataset

90   encompasses parameters such as sea surface temperature, cloud cover, air pressure, wind, specific humidity, evaporation, precipitation, and heat flux. The initial data of the model are introduced in the following ensemble experimental design section.

The tidal elevation forcing is composed of 8 major tidal components (M_2, S_2, N_2 K_2, K_1, O_1, P_1, and Q_1) derived from the TPXO8 database (Egbert & Erofeeva, 2002).

95

2.2 Ensemble Experiments design

We first used a control run to analyze the temperature, salinity, and velocity around the Qingdao cold water mass. Additionally, we conducted two further model experiments. One experiment was performed with tidal forcing turned off to examine the effect of tides on the Qingdao cold water mass, and another experiment was performed with wind forcing turned 100 off to test the effect of the wind.

Each ensemble experiment, the control run ensemble, no-tide ensemble, and no-wind forcing ensemble consisted of 4 simulations of 2019, initialized at fourteen, twelve, ten, and two months earlier, respectively, to 1st Jan. 2019. In each ensemble, the initial conditions of the four simulations are taken from 1st Nov. of the 7th year, 1st Jan. of the 8th year, 1st Mar. of the 8th year, and 1st Nov. of the 8th year of the separate 9-year climatological simulation. Note that we conducted an 105 independent 9-year simulation. The results for the year 2019 were used for further analysis. The model ending date is 31st December 2019. The model output interval is three hours. A more thorough description of the ensemble simulation configuration can be found in Lin et al. (2022).

Previous work (Lin et al. 2022, 2023) indicated that deviations exist within the ensemble members if the ensemble simulations are conducted with almost the same model configuration except for slight perturbations in the initial conditions. 110 Hence, in this study, we first test whether the variation caused by external forcings (tidal or wind forcings) is random. For instance, at a randomly selected grid node, in the control run, the node temperatures are $4\,°C$, $4.5°C$, $5°C$, and $6°C$ for the four ensemble members. When the tidal forcing is turned off, the temperature increases to $7°C$, $7.5°C$, $7°C$, and $8°C$. In this case, for both the control run and the run without tidal forcing, if only the first simulation member is considered (namely, $4°C$ for the control run and $7°C$ for the no-tide experiment), then the temperature of this grid node increases by $3°C$ when the 115 tidal forcing is turned off. However, these results are not different if we consider the mean temperature of this grid node's ensemble. Therefore, we conducted a t test to evaluate the statistical significance of the difference between the control run and the no-tide ensemble (or the no-wind ensemble). In this test, the null hypothesis is that the ensemble mean temperature in the control run and the no-tide ensemble (or the no-wind ensemble) are the same. The t test is done for the ensemble monthly mean for May. The results (shown in Supplemental Figs. A2 and A3) demonstrate that the difference between the 120 control run and the no-tide ensemble (or the /no-wind ensemble) is significant, especially where the intra-ensemble deviations are large. In this study, the ensemble means are used for the following analysis.

3. Result

3.1 Model validation

125 The model-simulated elevation, temperature, salinity, and circulation patterns were validated by Huang et al. (2019) and Lin et al. (2022, 2023). In this study, we focus directly on the analysis and discussion of the Qingdao cold water mass.

3.2 Temperature and Salinity of the Qingdao Cold Water Mass

The Qingdao cold water mass emerges in spring (from March to June) and is located northeast of Qingdao, the center of the

130   cold pool within the range of 120°30′-123°00′E，35°00′-36°30′N. Fig. 1 shows the temperature distribution at a depth of 25 m around the Qingdao cold water mass. In March, the cold water carried by the Bohai coastal current approaches the area around the Shandong Peninsula, gradually evolving to become the Qingdao cold water mass, but the isotherms did not close, and the Qingdao cold water mass structure did not form at this time (not shown). In April, a low-temperature tongue enveloped by an 8°C isotherm occurs north of 35°45′N and east of 121°45′E, accompanied by a temperature gradient.

135   During this period, the high-temperature water transported by the northwest path of the Yellow Sea warm current remains in the western region of the South Yellow Sea, forming an apparent ocean front with the Qingdao cold water mass (Fig. 1a). Moreover, the shape of the cold water masses has a northeast–southwest direction, which is similar to the direction of the Bohai coast current. In May, the location of the cold water mass center does not change at a depth of 25 m (Fig. 1b). Combined with the salinity results shown in Fig. 2, it is clear that the temperature and salinity are relatively low around the

140   Shandong Peninsula. Low-salinity water intrudes toward the south, and the intrusion direction is northeast–southwest, which is consistent with the results reported by Diao et al. (Diao, 2015). The low-temperature and low-salinity water tongue along the northeast of the Shandong Peninsula merges with the ambient warm water left by the Yellow Sea cold water mass beginning in winter. In June (Fig. 1c), the temperature increases as the solar radiation increases, accelerating the merging of warm and cold water and causing the Qingdao cold water mass to disappear. Figs. 15a and 15d present the vertical

145   temperature distribution of the Qingdao cold water mass along the 35.625 and 35.75°N profiles in May, revealing that the center of the cold water mass is at 122.4°E, and there is an evident thermocline, which prohibits heat transport from the surface to the water below. Additionally, the thermodynamic driving force for the formation of the Qingdao cold water mass is this strong thermocline. In summary, the Qingdao cold water mass starts to merge in April, continues to develop in May, is accompanied by a strong temperature gradient, and disappears in June. The cold water mass center is at 122.75°E 36.15°N,

150   and the shape of the cold water mass has a northeast–southwest orientation.
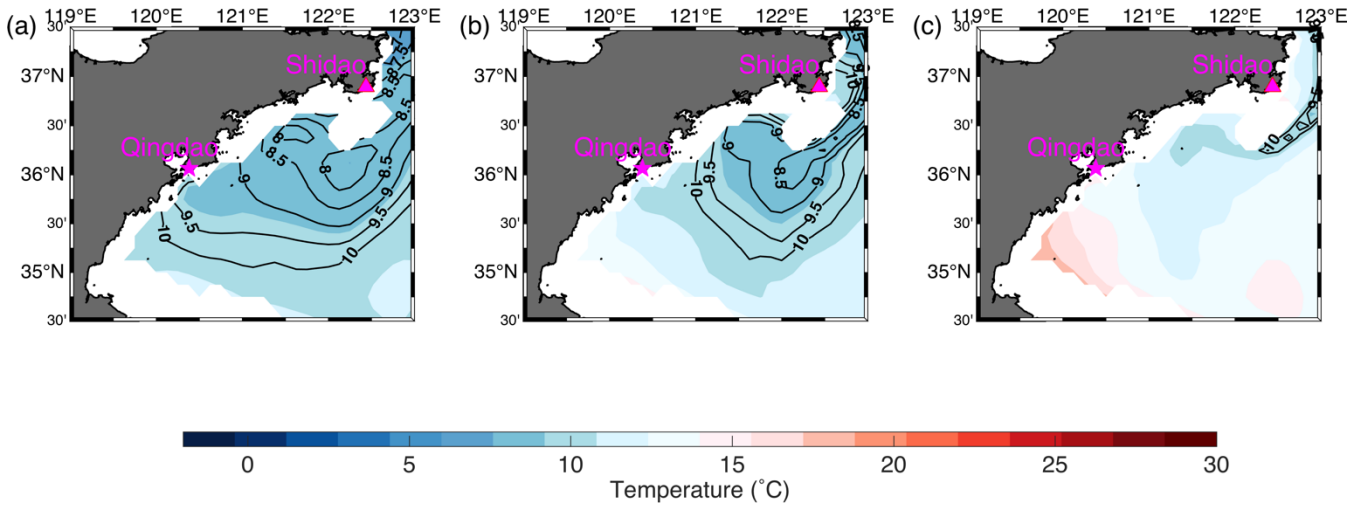
Figure 1. The monthly temperature evolution of the Qingdao cold water mass from April to June at a depth of 25 m. Figs. 1a, b, and c show the temperature distributions of the peaks of the Qingdao cold water mass (April), the gradual disappearance (May), and the complete disappearance (June), respectively. To clearly present the temperature distribution, the thermoclines between 8 and 10 are marked with 0.5 intervals.
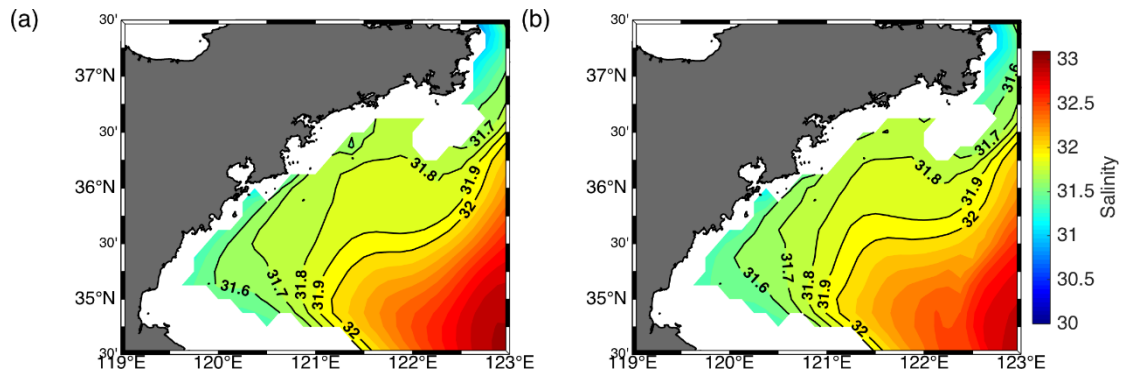

Figure 2. The monthly mean salinity around the Qingdao cold water mass in April (Fig. 2a) and May (Fig. 2b) in the 25 m layer.

3.3 Circulation pattern

An anticyclonic structure exists near the Qingdao cold water mass. Fig. 3 shows the circulation at a depth of 25 m from April to July. In April, the anticyclonic structure is not closed. In May, a southeast monsoon prevails near the Shandong Peninsula, and a northward current can be seen along the Shandong Peninsula coastline, meeting the southward current between 122 and 123˚E. In May and June, the anticyclonic structure closes, and the northeastward flow on the west side of the anticyclonic structure is stronger than the southwestward current on the east side. The center position of the anticyclonic circulation is 122.4˚E, 35.5˚N, and the velocity at the center of the anticyclonic circulation is very slow. In July, the anticyclonic circulation disappears when the southward current is strengthened (not shown). The above simulation results are consistent with previous works (Xu & Zhao, 1999; F. Zhang et al., 1987). As the water depth is shallow in the western

6

portion of the anticyclonic circulation and the dominant southward monsoon, the current velocities in the western part of the anticyclonic gyre are greater than those in the eastern part.
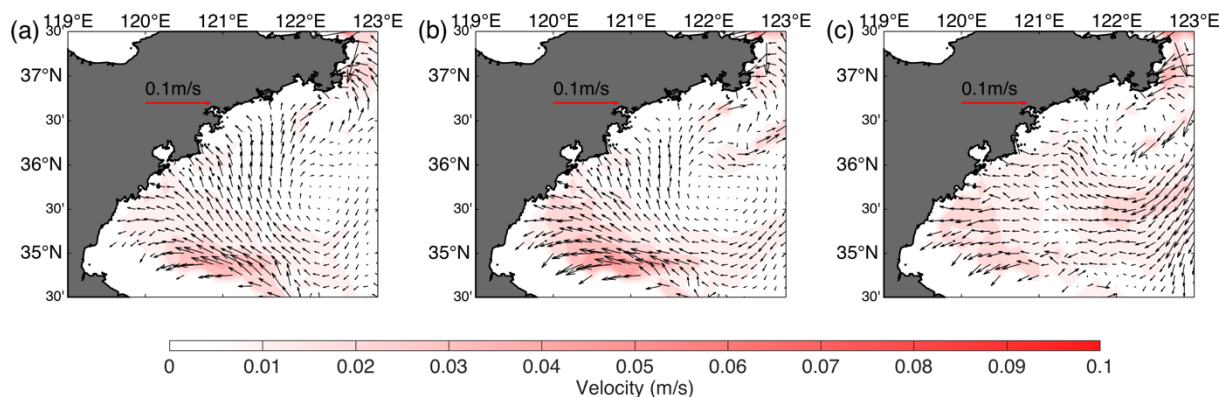
170

Figure 3. The horizontal circulation distribution around the Qingdao cold water mass (25 m layer) in April (a), May (b), and June (c).

The three-dimensional circulation pattern overlapped with temperature is shown in Fig. 4. There is a cold water mass center
175   in the 25 m layer, and the anticyclonic structure can still be observed at depths of 30 and 35 m. However, at depths greater than 35 m, the anticyclonic structure no longer exists. The circulation structures in different layers are not consistent, reflecting the baroclinic features of the current fields. The location and center of the cold water mass generally coincide with the position and center of the anticyclone, meaning that the Qingdao cold water mass is less affected by horizontal disturbances. At depths of 25, 30, and 35 m, the velocity increases as the temperature gradient around the edge of the cold
180   pool increases. The unique anticyclonic gyre structure hinders horizontal heat transfer, and this could serve as the dynamic mechanism for the formation of the Qingdao cold water mass (Huang et al., 2019).
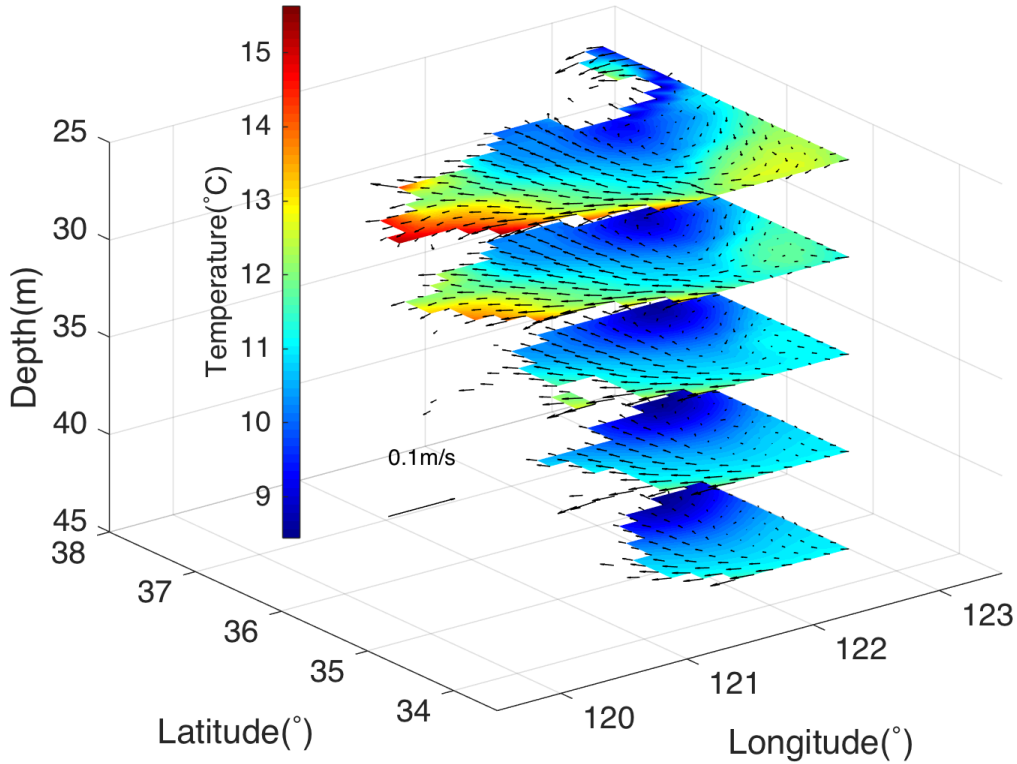
Figure 4. Three-dimensional structure of the Qingdao cold water mass in May at depths of 25 m, 30 m, 35 m, 40 m, and 45 m.

3.4 Momentum balance

$$\frac{\partial u}{\partial t} + u\frac{\partial u}{\partial x} + v\frac{\partial u}{\partial y} + w\frac{\partial u}{\partial z} - fv = -\frac{1}{\rho_o}\frac{\partial(p_H + p_a)}{\partial x} + \frac{\partial}{\partial z}\left(K_m\frac{\partial u}{\partial z}\right) + F_u \qquad (1)$$

$$\frac{\partial v}{\partial t} + u\frac{\partial v}{\partial x} + v\frac{\partial v}{\partial y} + w\frac{\partial v}{\partial z} - fu = -\frac{1}{\rho_o}\frac{\partial(p_H + p_a)}{\partial y} + \frac{\partial}{\partial z}\left(K_m\frac{\partial v}{\partial z}\right) + F_v \qquad (2)$$

To show the general pattern of the fundamental forces around the Qingdao cold water mass anticyclonic circulation region, we conduct a momentum balance diagnostic (see equations (1) - (2)). Taking the zonal direction as an example (equation (1)), the total pressure gradient term is $-\frac{1}{\rho_o}\frac{\partial(p_H + p_a)}{\partial x}$, which is composed of the barotropic pressure gradient force $\frac{1}{\rho}\frac{\partial\zeta}{\partial x}$ induced by sea level and the baroclinic pressure gradient force $\frac{1}{\rho}\frac{\partial}{\partial x}\int_z^\zeta \rho g dz$ induced by density; the Coriolis force $-fv$; the vertical friction term $\frac{\partial}{\partial z}\left(K_m\frac{\partial u}{\partial z}\right)$; the local velocity time variation term $\frac{\partial u}{\partial t}$; the horizontal advection term $u\frac{\partial u}{\partial x} + v\frac{\partial u}{\partial y}$; the vertical advection term $w\frac{\partial u}{\partial z}$; and the horizontal friction term F_u.

In both the 25 m (Fig. 5) and 40 m (Fig. 6) layers, the terms for the barotropic pressure gradient, baroclinic pressure gradient, Coriolis force, and vertical friction are dominant, and the other terms are far smaller (not shown). The barotropic gradient

force is greater than the baroclinic gradient force and is balanced by the joint effects of the opposing baroclinic pressure gradient force, Coriolis force, and vertical friction force. Vertical friction is induced by wind stress from the surface layer (Fig. A1) and bottom friction from the bottom layer. Because of the strong winds and shallow topography around the Qingdao cold water mass, the vertical friction term plays a role, especially east of 122°E. In May, the southwest wind stress

200   (Fig. A1) contributes to the northern current. Since the depth around the Qingdao cold water mass is relatively shallow, the friction caused by the tidal current and topography extends from the bottom layer to the middle layer, connecting with the wind stress from the surface layer, especially on the western side. Because there is vertical friction, the geostrophic balance no longer exists, especially in areas close to the coast. We will address this issue in section 3.5.
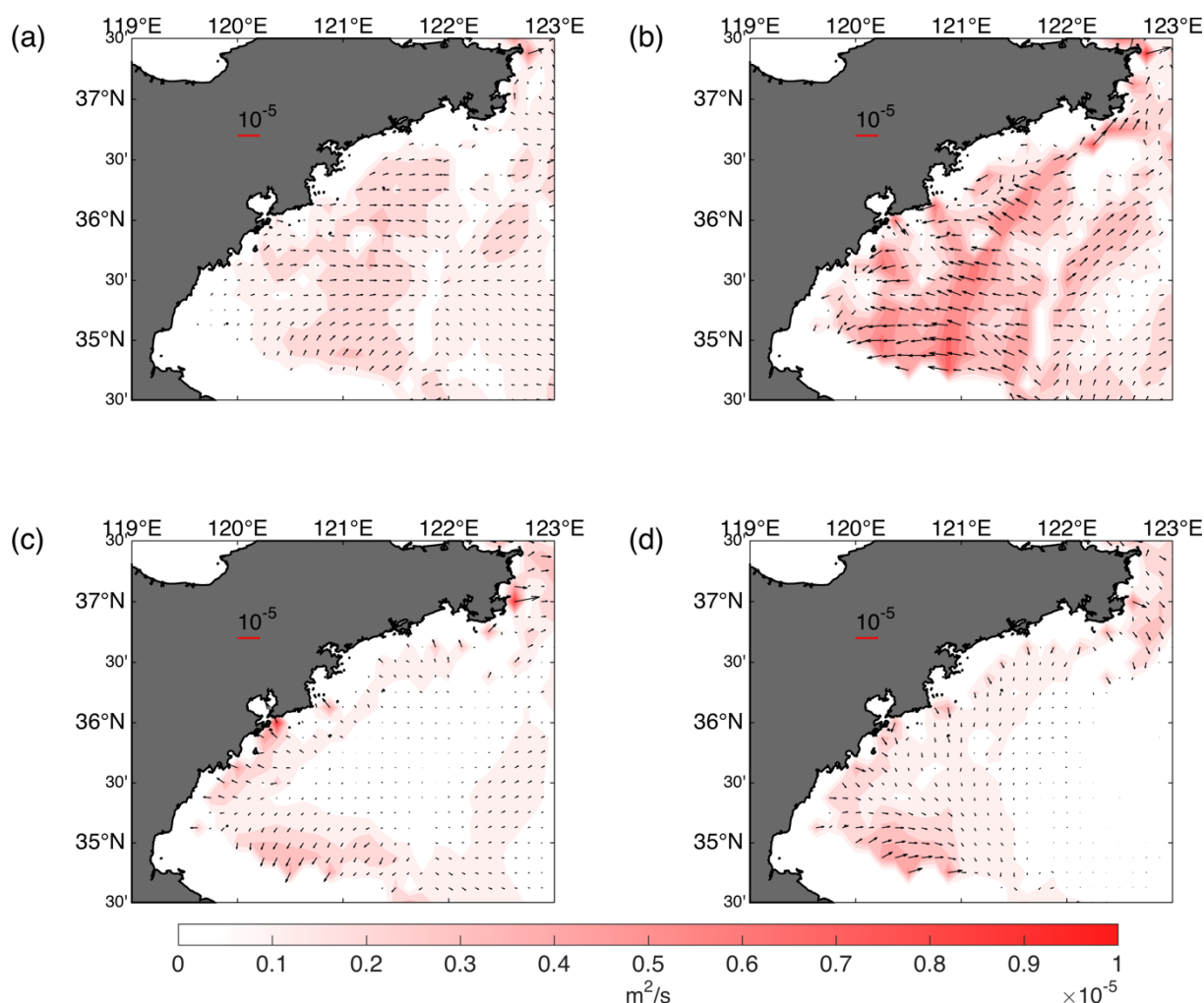
205   **Figure 5. Horizontal distribution of momentum terms (monthly mean for May) at a depth of 25 m: (a) Coriolis force, (b) barotropic pressure gradient force, (c) baroclinic pressure gradient force, and (d) vertical friction force. The color represents the magnitude of the momentum term.**
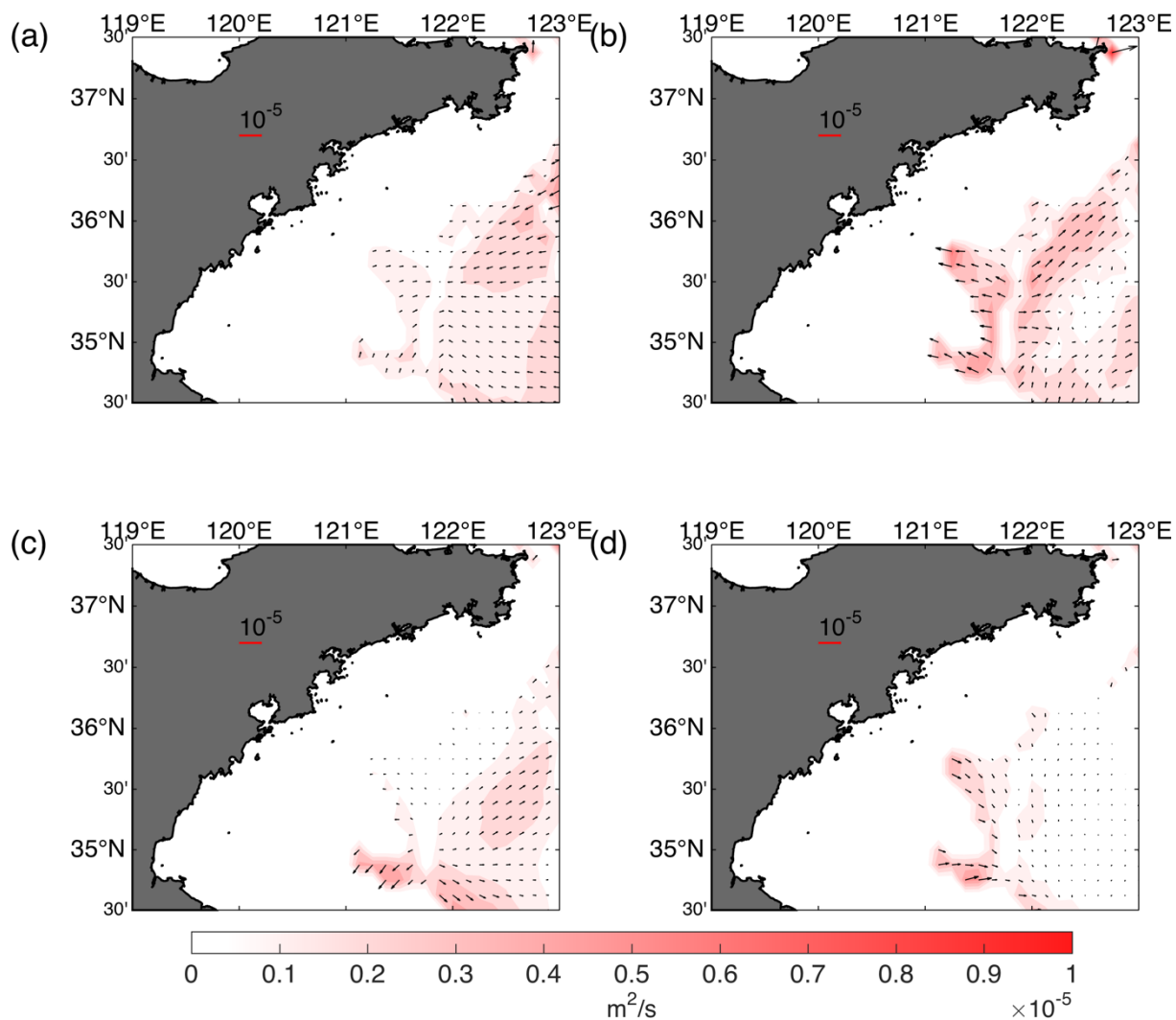
Figure 6. The same as Fig. 5, but for 40 m layer.

210 **3.5 Determination of whether the anticyclone circulation pattern is associated with the Qingdao cold water mass**
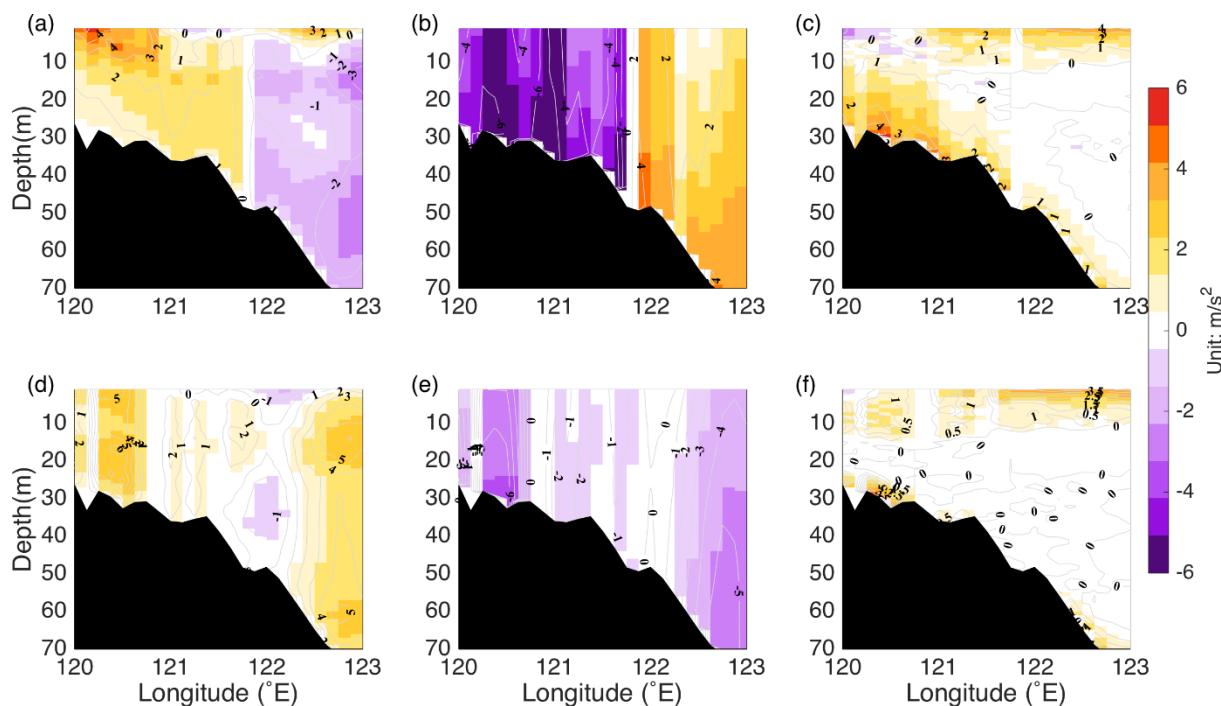
Figure 7. Vertical distribution of zonal momentum terms along the 35.5°N profile of the control run (a, b, c) and the no-tide experiment (e, f, g). (a, d) Coriolis force, (b, e) total pressure gradient force, (c, f) vertical friction force. The magnitude of the momentum terms has a time of 10^6 for visualization.

215 To further analyze the anticyclonic circulation around the Qingdao cold water mass, we show the vertical distributions of the Coriolis force, the total pressure gradient force, and the vertical friction force along the 35.5°N profile (Fig. 7). In the surface layer (0-10 m), to the west of 123°E, the total pressure gradient force is balanced by the combined effect of the Coriolis force and surface wind stress. In the middle layer (10-30 m), the Coriolis force is positive west of 122°E when the total pressure gradient is negative, while the region east of 122°E shows the opposite behavior. However, west of 122°E, the Coriolis force

220 is not identical to the total pressure gradient force, indicating that the vertical friction force cannot be ignored, which is consistent with the conclusion drawn from the horizontal momentum balance distribution. The Ekman ratio is the ratio of the friction and Coriolis terms and represents the relative significance of the friction force (Fig. 8). The Ekman ratio is usually high in coastal areas. Fig. 8 shows that the Ekman ratio is much higher along the bottom layer in the control run, which indicates that the friction term again plays a significant role around the Qingdao cold water mass. Most importantly, the

225 geostrophic balance is not valid west of 122°E, where the anticyclonic circulation exists on the western side.

Because the geostrophic balance is not satisfied in the western portion of the anticyclonic circulation, the anticyclonic circulation structure is not a direct result of the density gradient fronts, which are induced by the temperature and salinity gradients. This explains why an anticyclonic circulation appears around a cold temperature center caused by the Qingdao cold water mass. If the geostrophic balance is satisfied, then in the North Hemisphere, there should be an anticlockwise

230   cyclonic circulation structure around a cold temperature center. The vertical friction completely disrupts the geostrophic

balance.

To some extent, the anticyclonic circulation is the dynamic reason for the Qingdao cold water mass; this type of anticyclonic

structure prohibits heat transfer between the cold temperature center and the surrounding water column (Huang et al., 2019),

but the anticyclonic circulation is not caused by the special temperature and salinity structure around the Qingdao cold water

235   mass.
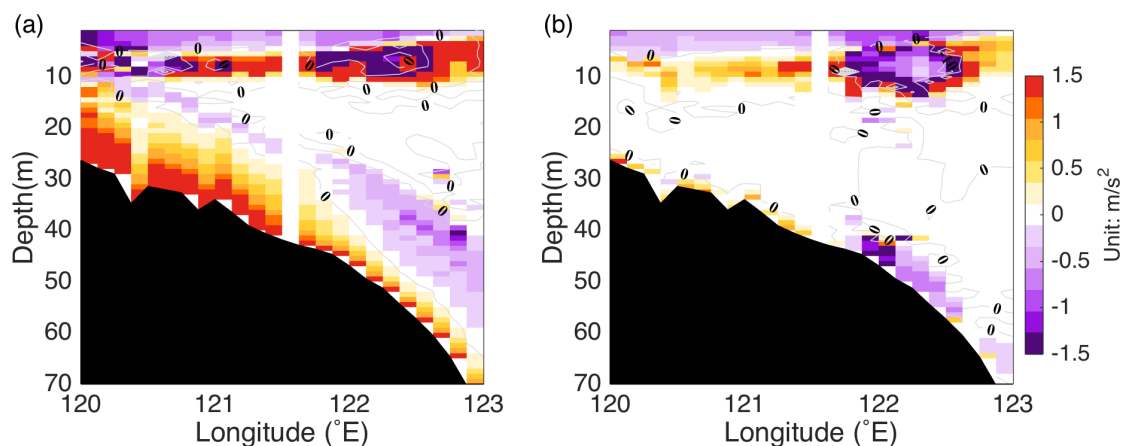
Figure 8. Vertical distribution of the Ekman ratio along the 35.5°N profile of the control run (a) and the no-tide experiment in the zonal direction.

4. Discussion

4.1 Tidal effects

In the Yellow Sea, tidal forcing plays a significant role in the local circulation and modulates dissipation, vertical mixing,

and tidal energy (Choi, 1980; Choi et al., 2003; Moon et al., 2009; C. Xia et al., 2006). A no-tide simulation is conducted to

analyze the tidal forcing effect on the anticyclonic circulation around the Qingdao cold water mass. Fig. 9 shows the

245   circulation pattern of the no-tide experiment in May at a depth of 25 m and the current deviations between the no-tide

experiment and the control run; the results reveal that the circulation is different from that in the control run. Northward

currents are present on the western side (to the west of 122°E) in the control run and in the no-tide experiment, but the

magnitudes are significantly greater in the no-tide experiment. At the center of the anticyclonic circulation, changes in the

current are not evident. When the tidal forcing is turned off, the eastern side of the anticyclonic circulation direction reverses,

250   changing from a southward current (in the control run, see Fig. 3b) to a northward current. The clockwise circulation pattern

disappears in the no-tide experiment. In the no-tide experiment, the current magnitude significantly increased throughout the

region. This is because the friction is much lower than that in the control run, which is indicated by the momentum balance results (Fig. 10).

The momentum diagnostic of the no-tide experiments shows that the magnitude of the velocity decreases compared with that of the control run. When tidal forcing is not considered, the vertical friction along the bottom layer becomes much smaller than that in the control run. Without tidal forcing, east of 122°E, the total pressure gradient and Coriolis terms change direction, and this is combined with a change in the circulation direction, indicating the significance of the tides around the anticyclonic circulation. In addition, the magnitude of the current in the entire region significantly increases, which is not realistic, illustrating that the dissipation and friction caused by tidal forcing are important for modulating circulation in anticyclonic areas.
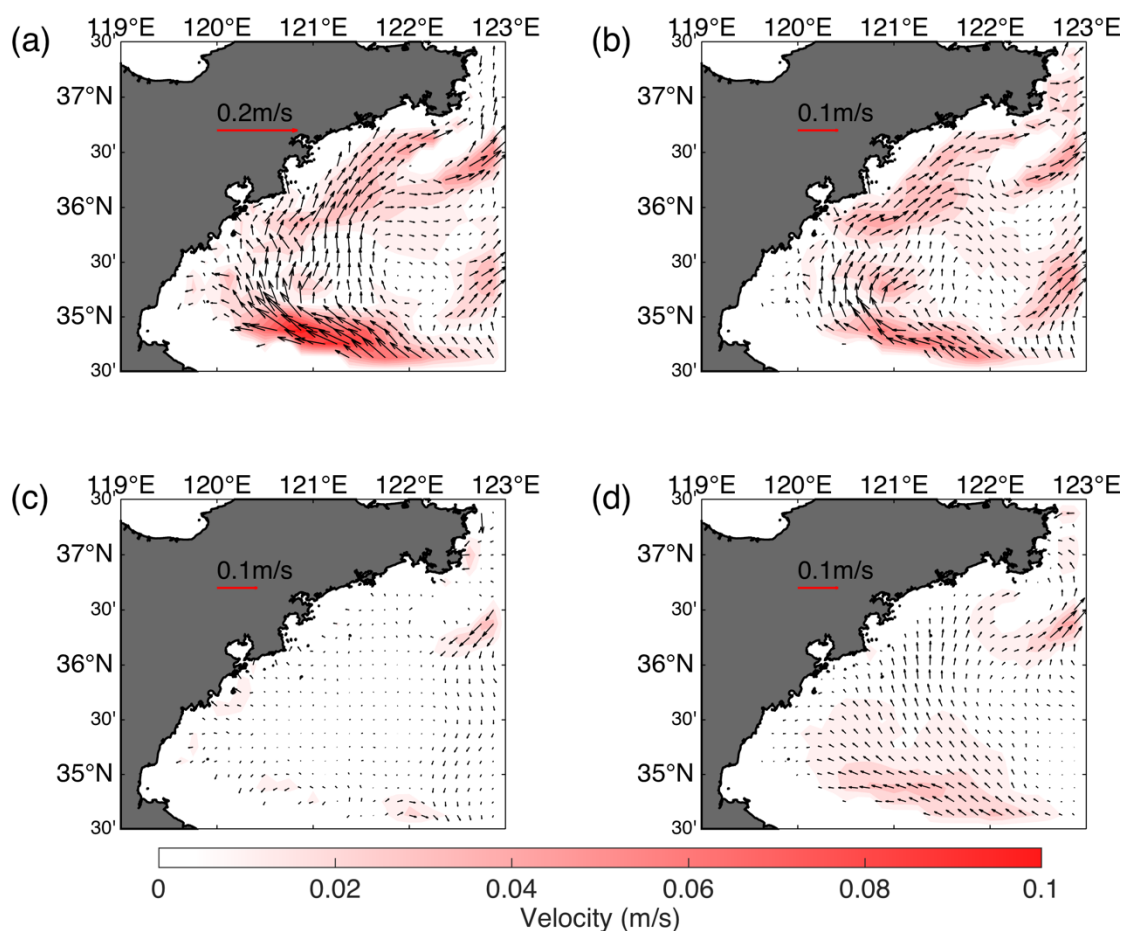

Figure 9. The impacts of tidal forcing and wind forcing on anticyclonic circulation in May at 25 m; (a) the circulation pattern of the no-tide experiment, (b) the difference between the no-tide experiment and the control run (no-tide experiment minus control run), (c) the circulation pattern of the no-wind experiment, and (d) the difference between the control run and the no-wind experiment (control run minus no-wind experiment).
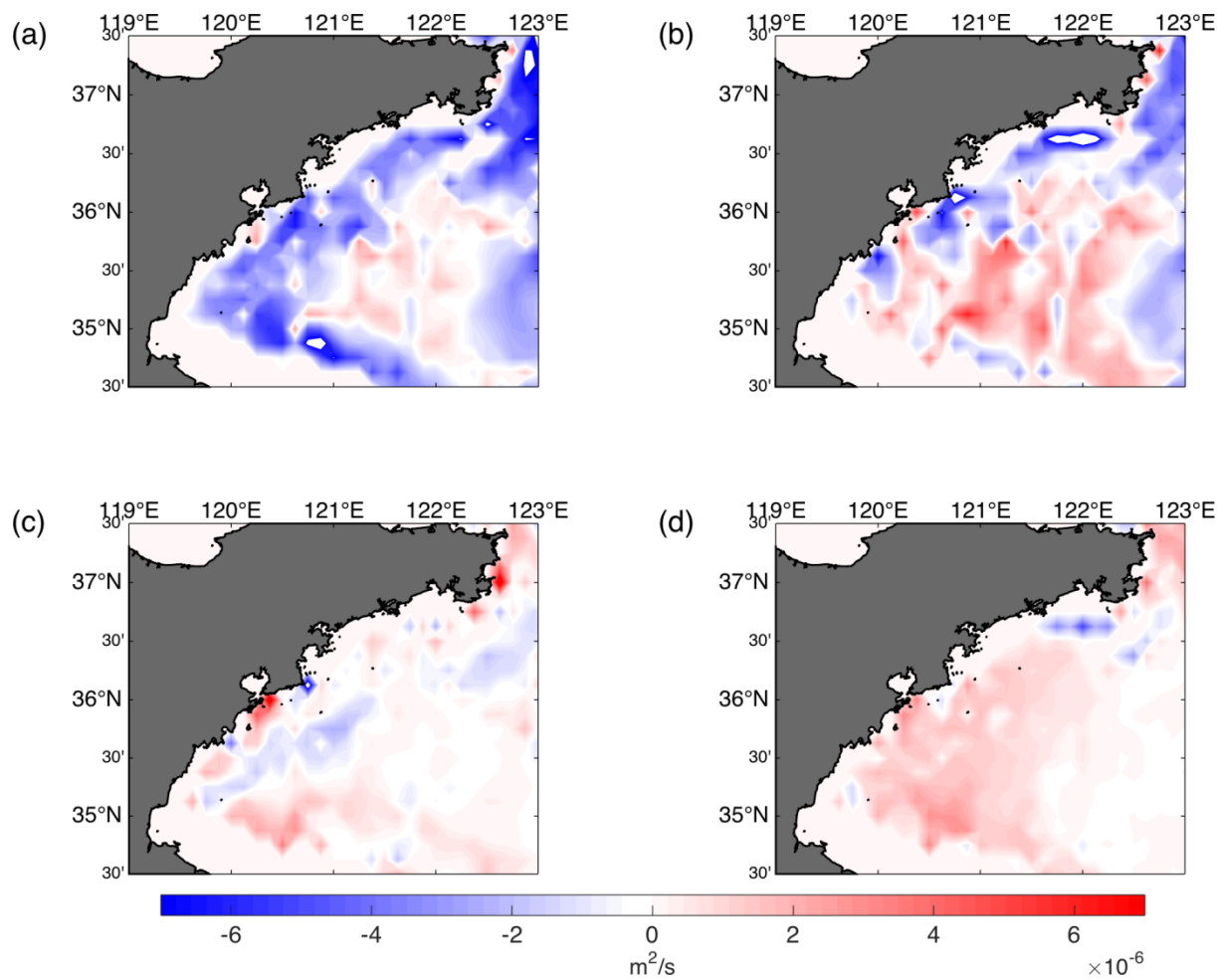
Figure 10. The momentum balance terms between the control run and the no-tide experiment at 25 m (control run minus no-tide experiment; monthly mean for May). The (a) Coriolis force, (b) barotropic pressure gradient force, (c) baroclinic pressure gradient force, and (d) vertical friction term.

4.2 Wind effects

14
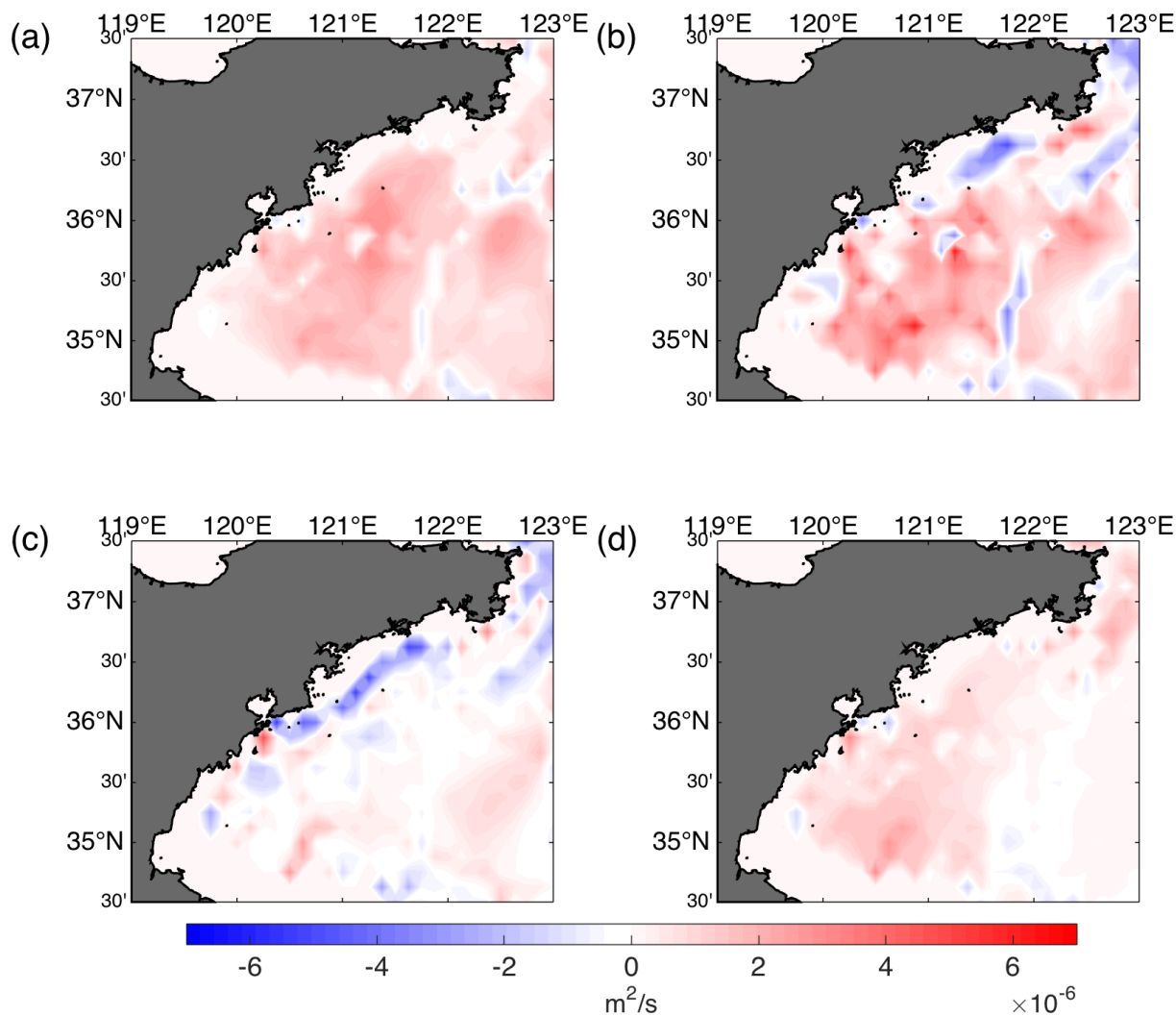
Figure 11. The momentum balance terms between the control run and the no-wind experiment at 25 m (control run minus no-wind experiment; time average over two M₂ tide cycles). The (a) Coriolis force, (b) barotropic pressure gradient force, (c) baroclinic pressure gradient force, and (d) vertical friction term.
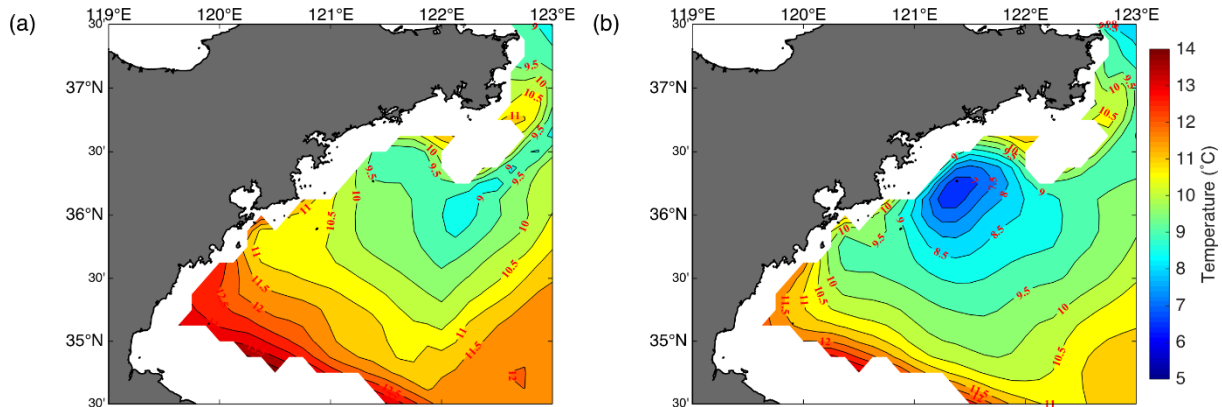
Figure 12. The horizontal temperature distribution at 25 m in the control run (a) and the no-wind experiment (b) (monthly mean for May).
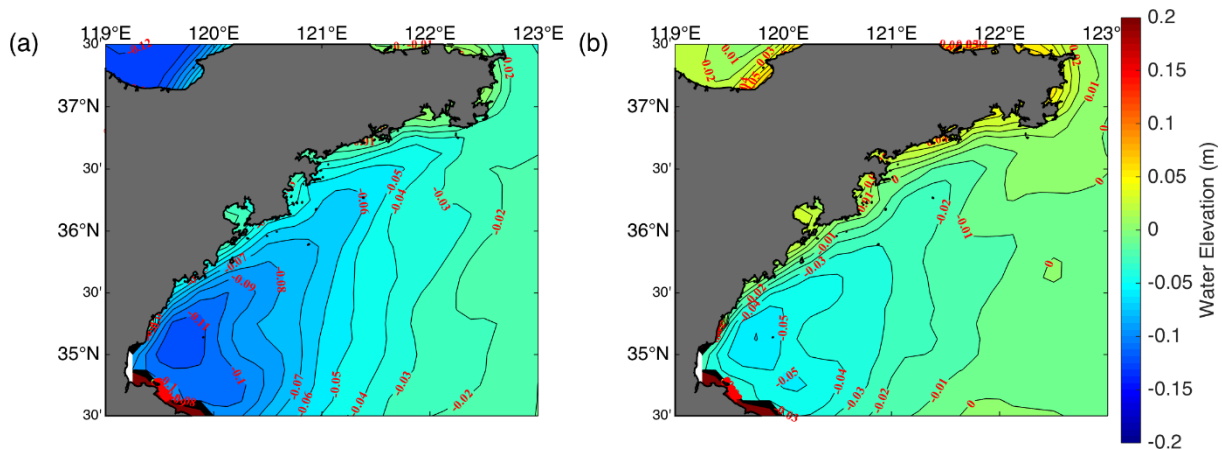

Figure 13. The surface elevation distributions of the control run (a) and the no-wind experiment (b). The monthly mean for May.

Xu and Zhao (1999) demonstrated the effect of wind on the anticyclonic circulation around the Qingdao cold water mass based on a 2D numerical model, but a more thorough discussion is needed. Therefore, we conducted a no-wind experiment to examine the effect of wind on the anticyclonic circulation structure. The results show that wind is a dominant driving force for clockwise circulation. The general magnitude of the current weakens, particularly on the western side of the anticlockwise circulation (northward current), confirming again that the southerly wind along the Shandong Peninsula is the cause. In contrast, the influence of wind on the eastern side of the circulation is minor, as shown in Figs. 9c and 9d. The direction and magnitude of the eastern side are similar to those of the control run.

To compare the momentum changes and further analyze the wind forcing effect in this area, we show the difference in the momentum changes between the control run and the no-wind experiment (control run minus the no-wind experiment, Fig. 11). The Coriolis force decreases because of the weaker current when the wind forcing is turned off. The barotropic gradient force increases when wind forcing is considered, indicating that the variation caused by water elevation is greater with wind

16

forcing. The surface elevation is shown in Fig. 13. With a southerly wind, the water surface is lower west of 121°E in the control run, indicating that the pressure gradient force distribution varies in the no-wind experiment. On the other hand, in the absence of mixing caused by surface winds, the temperature of the Qingdao cold water mass decreased by 2°C, resulting in a decrease in the baroclinic pressure gradient force around the location of the Qingdao cold water mass in the no-wind

300   experiment. The vertical friction is somewhat decreased because of the lack of wind stress in the no-wind experiment.

4.3 Upwelling

Vertically, upwelling occurs from the surface layer to the bottom layer near the Qingdao cold water mass, accompanied by relatively weak downwelling at the surface layer. Fig. 14 shows the vertical circulation structure in May at 35.75°N and

305   122.5°E, which is the horizontal center of the anticyclonic gyre. Upwellings occur near the frontal zones (121.5-122°E and 122.625-123°E) on the eastern and western sides of the Qingdao cold water mass, respectively. The seawater lifted by upwelling from the western and eastern sides of the cold pool converges toward the center, forming a downwelling in the surface layer at 122.5°E, but this downwelling is weak compared with the strength of upwelling.

We hypothesize that the upwelling in the western portion (121.5-122°E) is influenced mainly by wind forcing, which is

310   Ekman upwelling. For the eastern portion (122.625-123°E), the wind forcing still plays a role, but for the eastern portion, tidal forcing contributes more to upwelling. The tidal mixing front generates a pressure gradient force, which strengthens the upwelling intensity on the east side. To test our hypothesis, we further analyzed the vertical circulation with two profiles (35.625°N and 35.75°N) in May of the control run, the no-tide experiment, and the no-wind experiment (Fig. 15). To clearly visualize the vertical circulation, a separate vertical speed contour map overlapped with the temperature contours is plotted
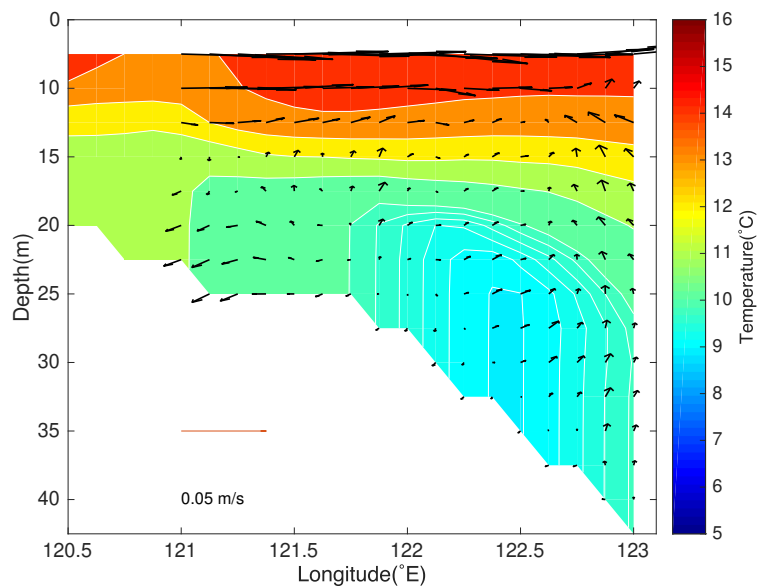
315   (Fig. 16).

17

Figure 14. The temperature and zonal-vertical current along the 35.75°N profile in May. For better visualization, the vertical velocity is multiplied by 1000 (unit: m/s), as in Figs. 15 and 16.
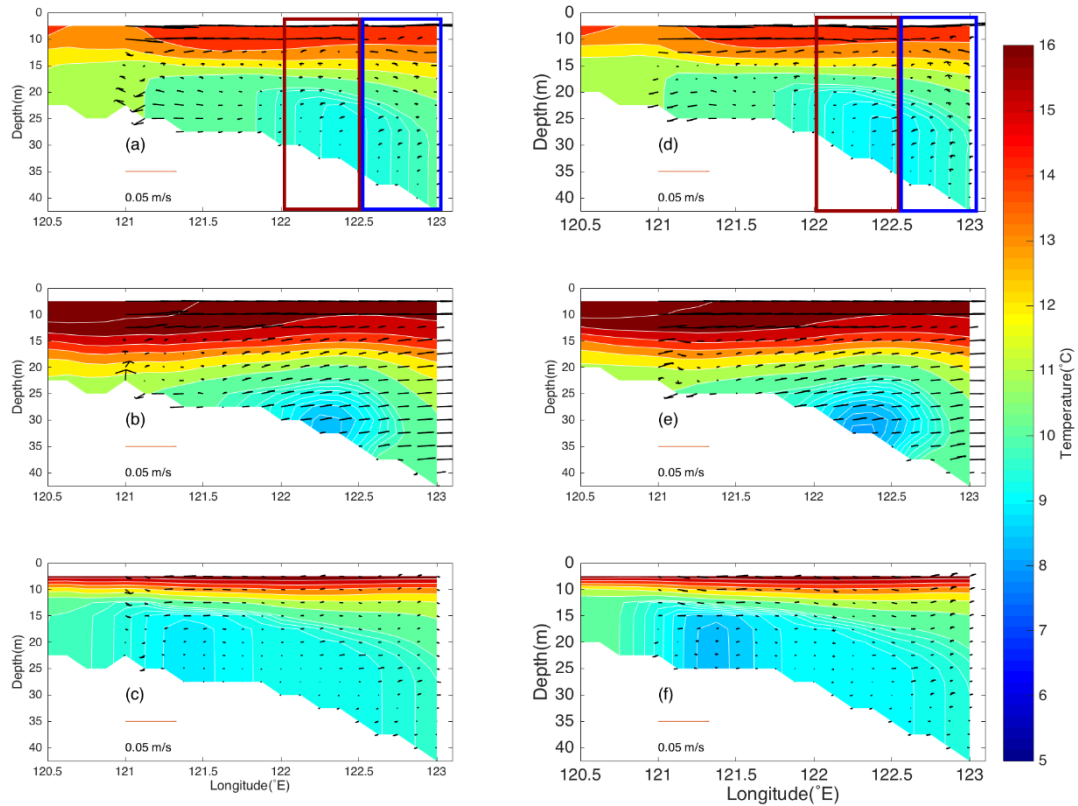
320

Figure 15. The temperature and zonal-vertical current around the Qingdao Cold Water mass in May at 35.625˚N (a, b, c) and 35.75˚N (d, e, f) profiles; the first (Figs. 15a and d), the second (Figs. 15b and e), and the third row (Figs. 15c and f) represent the simulated results of the control run, No-tide experiment, and the No-wind experiment.

325 Figure 15 shows that in the control, an eastward flow exists toward the sea surface at west of 122.375°E (red rectangle), and a westward flow exists toward the sea surface in the region east of 122.625°E (blue rectangle).

A comparison of Fig. 16a/16d and 16c/16f reveals that upwelling cycles occur in the red and blue rectangles in the control run (Fig. 16a/16d), but in the no-wind experiment (Fig. 16c/16f), the magnitude of upwelling cycling in the red rectangle decreases in Fig. 16c along with changes to downwelling in Fig. 16f. In contrast, the impact of the wind forcing on

330 upwelling in the eastern portion (122.5-123°E) is weaker, as the upward velocity still occurs between 122.5 and 123°E (Figs. 16c and 16f). Therefore, the wind forcing has a significant impact on the upwelling in the western portion of the Qingdao cold water mass (122-122.375°E).

In the no-tide experiment (Figs. 16b and 16e), the magnitude of upwelling is the same as that in the control run on the west side of the Qingdao cold water mass (to the west of 122.375°E), but on the east side of the Qingdao cold water mass, the

335 magnitude of the upwelling decreases. Therefore, we conclude that tidal forcing mainly affects upwelling on the west side of

the Qingdao cold water mass. Additionally, the zonal velocity greatly increases when the tidal forcing is turned off, mainly because the friction decreases in the no-tide experiment, as discussed in section 4.1.
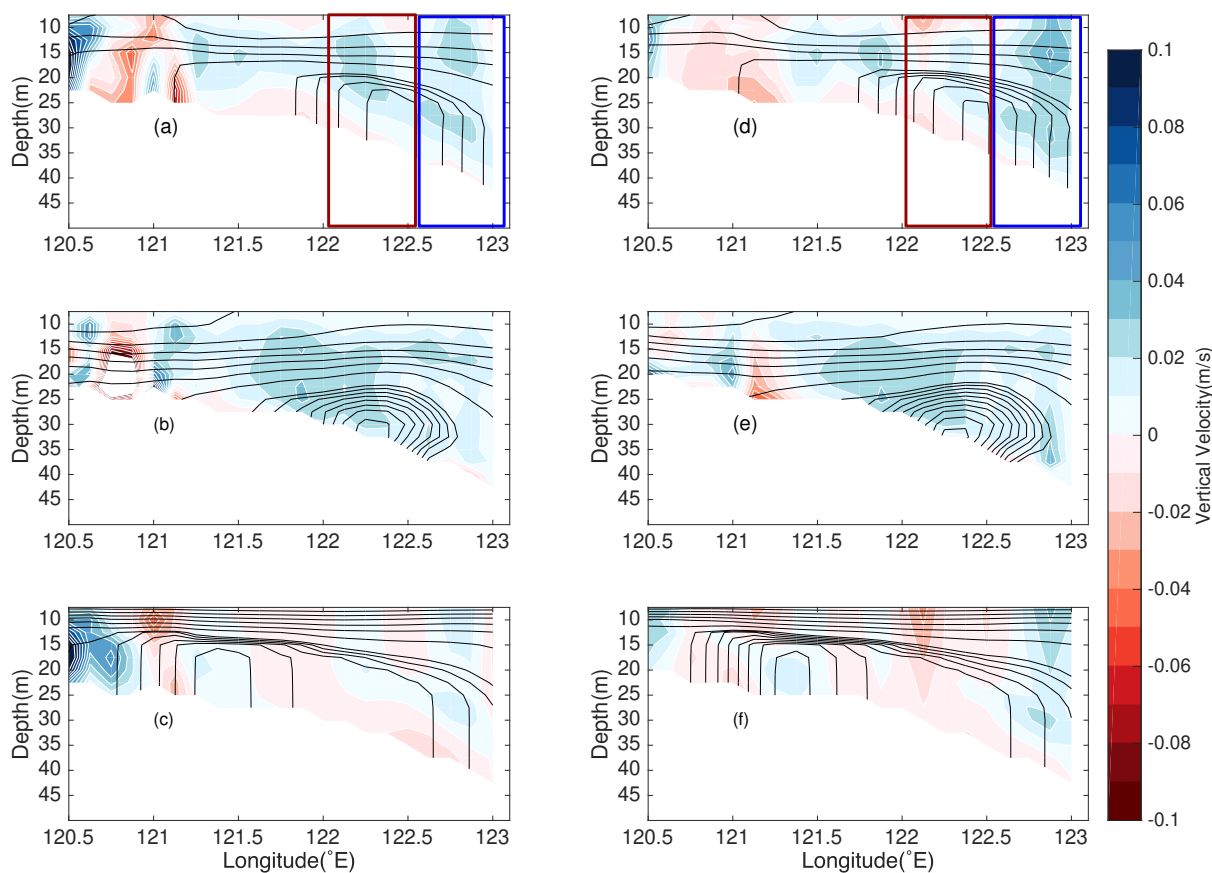
Figure 16. These graphs are the same as those in Fig. 15. However, the color represents the vertical velocity, and the contour lines are temperature contours.

These results validate our hypothesis that upwelling in the western portion (121.5-122°E) is influenced mainly by wind forcing; for the eastern portion (122.625-123°E), wind forcing still play a role, but tidal forcing contributes more to upwelling. Lü et al. (2010) explained the tidal effect on upwelling, which indicates that the tide-induced front in the control run generates a relatively large baroclinic pressure gradient, which further triggers distinct upwelling.

Previous authors have also studied upwelling and vertical secondary circulation in the Bohai and Yellow Seas, and it was revealed that upwelling usually occurs in shallow areas along coasts, for example, the Subei area and the region near the Korean Peninsula (Lü et al., 2010; Q. Wei et al., 2019); however, a refined analysis of the Qingdao cold water mass is still needed. Hence, in this study, we analyzed the upwelling structure of in this area and explored the effects of wind and tidal forcings on upwelling.

4.4 Comparison between the Yellow Sea basin-scale cyclonic circulation structure around the Yellow Sea cold water mass and the anticyclonic circulation structure around the Qingdao cold water mass

Cold water masses are often accompanied by unique circulation fields, and Hill's research indicated that cyclonic flow

355 structures frequently occur near cold water masses (1996). As described in the introduction, in the Yellow Sea region, except for areas near the seafloor and shallow water, a quasigeostrophic balance is achieved in both the bottom and middle layers. The ocean front in the bottom layer generates pressure gradient forces: in the western bottom layer of the Yellow Sea, the pressure gradient force is positive, while in the eastern bottom layer of the Yellow Sea, it is negative, resulting in the divergence of bottom layer seawater. Bottom layer divergence causes middle layer convergence. Since the middle layer flow

360 also satisfies quasigeostrophic relationships, a high-density center forms at the bottom center of the Yellow Sea, leading to the formation of a cyclonic flow field. However, due to the shallow depth near the Qingdao cold water mass, friction destroys the quasigeostrophic balance of the bottom and middle layers. The formation of horizontal circulation structures near the Qingdao cold water mass is different from that of the cyclonic flow field near the cold water mass in the Yellow Sea.

365 Based on the no-wind and no-tide experiment results, the wind forcing has an evident impact on the upwelling on the west side of the Qingdao cold water mass, and tidal forcing enhances upwelling on the east side of the Qingdao cold water mass (122.5-123°E).

5. Conclusion

370 Based on numerical models, the main characteristics and related dynamic processes of the local anticyclonic gyre around the Qingdao cold water mass during spring and summer were analyzed in this paper. The Qingdao cold water mass emerges in April and is fully developed in May, combined with an anti-clockwise gyre. Two major scientific questions mentioned in the introduction are answered: (1) The Qingdao cold water mass is not the direct reason for the anti-clockwise gyre around the Qingdao cold water mass. The geostrophic balance is not satisfied because the topography of the Qingdao cold water mass is

375 shallow, thus inducing strong vertical friction. Based on the momentum diagnostic results, the barotropic gradient force is balanced by the joint effects of the opposing baroclinic pressure gradient force, the Coriolis force, and the vertical friction force. (2) Both tidal forcing and wind forcing play roles in the horizontal anticyclonic gyre. When wind forcing is not considered, the current's general magnitude weakens, particularly on the western side of the anticlockwise circulation (northward current), confirming again that the southerly wind along the Shandong Peninsula is the cause of the northward

380 current on the west side of the Qingdao cold water mass. Additionally, when tidal forcing is not considered, the eastern side of the anticyclonic circulation direction reverses, changing from a southward current to a northward current. Vertically, the

tidal front causes a baroclinic pressure gradient force, which further triggers upwelling; wind forcing contributes to Ekman upwelling in the western portion (121.5-122°E).

385 *Author contributions.* LL formulated the carried out all simulations, alalyzed the results, and wrote the manuscript. HvS gave guidance and wrote the manuscript. DY helped with numerical model momentum balance output, gave guidance of the manuscript.

Competing interests. The contact author has declared that none of the authors has any competing interests.

Data availability. The datasets generated during and/or analyzed during the current study are available from the corresponding author on reasonable request.

References

395 Chen, C., & Cowles, G. (2006). AN UNSTRUCTURED-GRID, FINITE-VOLUME COASTAL OCEAN MODEL (FVCOM) SYSTEM. Advances in Computational Oceanograghy, 19(1).

Choi, B. H. (1980). A Tidal Model of the Yellow Sea and the Eastern China Sea. Korea Ocean Research and Development Institute. https://books.google.de/books?id=nQwIAQAAIAAJ

Choi, B. H., Eum, H. M., & Woo, S. B. (2003). A synchronously coupled tide–wave–surge model of the Yellow Sea. Coastal
400 Engineering, 47(4), 381–398. https://doi.org/10.1016/S0378-3839(02)00143-6

Diao, X. (2015). The study of Yellow Sea Warm Current, Yellow Sea Cold Water Mass and their evolution process in sping. Institute of Oceanology, Chinese Academy of Sciences.

Egbert, G. D., & Erofeeva, S. Y. (2002). Efficient Inverse Modeling of Barotropic Ocean Tides. Journal of Atmospheric and Oceanic Technology, 19(2), 183–204. https://doi.org/10.1175/1520-0426(2002)019<0183:EIMOBO>2.0.CO;2

405 Hill, A. E. (1996). Spin-down and the dynamics of dense pool gyres in shallow seas. Journal of Marine Research, 54(3), 471–486. https://doi.org/10.1357/0022240963213538

Ho, C., Wang, Y., Lei, Z., & Xu, S. (1959). A prelimenary study of the formation of Yellow Sea Cold Mass and its properties. Oceanologia Et Limnologia Sinica, 2(1), 11—15.

Huang, H., Chen, X., & Lin, L. (2019). Evolution and mechnism of the Qingdao Cold Water Mass. Oceanologia Et
410 Limnologia Sinica, 50(6), 1191–1200.

Hur, H. B., Jacobs, G. A., & Teague, W. J. (2000). Monthly variations of water masses in the Yellow and East China Seas. Journal of Oceanography, 56(3), 359.

Lin, L., Von Storch, H., Chen, X., Jiang, W., & Tang, S. (2023). Link between the internal variability and the baroclinic instability in the Bohai and Yellow Sea. Ocean Dynamics, 73(12), 793–806. https://doi.org/10.1007/s10236-023-01583-7

Lin, L., von Storch, H., Guo, D., Tang, S., Zheng, P., & Chen, X. (2022). The effect of tides on internal variability in the Bohai and Yellow Sea. Dynamics of Atmospheres and Oceans, 98, 101301. https://doi.org/10.1016/j.dynatmoce.2022.101301

Liu, G. M., Wang, H., Sun, S., & Han, B. P. (2003). Numerical study on density residual currents of the Bohai Sea in summer. Chin. J. Oceanol. Limnol., 21(2), 106–113.

Lü, X., Qiao, F., Xia, C., Wang, G., & Yuan, Y. (2010). Upwelling and surface cold patches in the Yellow Sea in summer: Effects of tidal mixing on the vertical circulation. Continental Shelf Research, 30(6), 620–632. https://doi.org/10.1016/j.csr.2009.09.002

Mellor, G. L., & Yamada, T. (1982). Development of a turbulence closure model for geophysical fluid problems. Reviews of Geophysics, 20(4), 851. https://doi.org/10.1029/RG020i004p00851

Moon, J.-H., Hirose, N., & Yoon, J.-H. (2009). Comparison of wind and tidal contributions to seasonal circulation of the Yellow Sea. Journal of Geophysical Research, 114(C8), C08016. https://doi.org/10.1029/2009JC005314

Wan, X. G., Bao, X., Wu, D., & Jiang, H. (2004). Numerical diagnostic simulation of summertime tide-induced, wind-driven and thermohaline currents in the Bohai Sea. Oceanologia Et Limnologia Sinica, 35(1), 47–53.

Wang, B., Hirose, N., Kang, B., & Takayama, K. (2014). Seasonal migration of the Yellow Sea Bottom Cold Water. Journal of Geophysical Research: Oceans, 119(7), 4430–4443. https://doi.org/10.1002/2014JC009873

Wei, H., Shi, J., Lu, Y., & Peng, Y. (2010). Interannual and long-term hydrographic changes in the Yellow Sea during 1977–1998. Deep Sea Research Part II: Topical Studies in Oceanography, 57(11–12), 1025–1034. https://doi.org/10.1016/j.dsr2.2010.02.004

Wei, Q., Wang, B., Yao, Q., Yu, Z., Fu, M., Sun, J., Xu, B., Xie, L., & Xin, M. (2019). Physical-biogeochemical interactions and potential effects on phytoplankton and Ulva prolifera in the coastal waters off Qingdao (Yellow Sea, China). Acta Oceanologica Sinica, 38(2), 11–23. https://doi.org/10.1007/s13131-019-1344-3

Xia, C., Qiao, F., Yang, Y., Ma, J., & Yuan, Y. (2006). Three-dimensional structure of the summertime circulation in the Yellow Sea from a wave-tide-circulation coupled model. Journal of Geophysical Research, 111(C11), C11S03. https://doi.org/10.1029/2005JC003218

Xia, J., & Xiong, X. (2013). Distributions and seasonal changes of water temperature in the Bohai Sea, Yellow Sea and East China Sea. Advances in Marine Science, 31(1), 55–68.

Xu, D., & Zhao, B. (1999). Existential proof and numerical study of a mesoscale anticyclonis eddy in the Qingdao-Shidao offshore. Acta Oceanologica Sinica, 2, 18–26.

445   Yu, F., Zhang, Z., Diao, X., Guo, J., & Tang, Y. (2006). Analysis of evolution of the Huanghai Sea Cold Water Mass and its relationship with adjacent water masses. Acta Oceanologica Sinica, 05, 26–34. https://doi.org/CNKI:SUN:SEAC.0.2006-05-002.

Yu, F., Zhixin, Z., Diao, X., Guo, J., & Ge, R. (2005). Analysis of water temperature distribution characteristics in the Southern Yellow Sea in spring. Advances in Marine Science, 23(3), 281–288.

450   Yuan, D., Li, Y., Qiao, F., & Zhao, W. (2013). Temperature inversion in the Huanghai Sea bottom cold water in summer. Acta Oceanologica Sinica, 32(3), 42–47. https://doi.org/10.1007/s13131-013-0287-3

Zhang, cunyi. (1986). Analysis of the strength and yearly vairations of Qingdao cold water-masses. Marine Sciences, 10(3), 48–51.

Zhang, F., Mao, H., & Leng, Y. (1987). Analysis of drift bottle and drift card experiments in Bohai Sea and Huanghai Sea
455   (1975–80). Chinese Journal of Oceanology and Limnology, 5(1), 67–72. https://doi.org/10.1007/BF02848524

Zhang, Q., Hou, Y., Cheng, M., Liu, X., & Yin, B. (2004). Variation Features in Qingdao Cold Water Mass Strength. Studia Marina Sinica, 46(1), 13–21.

Zhang, Q., Liu, X., Cheng, M., & Y, X. (2002). Characteristics and formation causes of Qingdao cold water mass. Chinese Journal of Oceanology and Limnology, 20, 303–308.

460   Zhang, Q., Yang, Y., & Cheng, M. (1994). An analysis of characteristics of thermohaline structures in the South Yellow Sea in spring. Haiyang Xuebao, 18(6), 50–55.

Zhang, Y., & Geng, X. (1989). Relationship between fishery and hydrological situation. Hydrological regime in Shandong coastal waters. Ji-nan:Shandong Map Press.

Zheng, D., & Zhang, R. (1983). Analysis of spring water masses in the sea area off Yantai, Weihai, and Shidao. Marine
465   Science Bulletin, 01, 61–68.

Zhou, F., Huang, D., Xue, H., Xuan, J., Yan, T., Ni, X., Zeng, D., & Li, J. (2017). Circulations associated with cold pools in the Bohai Sea on the Chinese continental shelf. Continental Shelf Research, 137, 25–38. https://doi.org/10.1016/j.csr.2017.02.005

Zhu, P., & Wu, H. (2018). Origins and transports of the low-salinity coastal water in the southwestern Yellow Sea. Acta
470   Oceanologica Sinica, 37(4), 1–11. https://doi.org/10.1007/s13131-018-1200-x
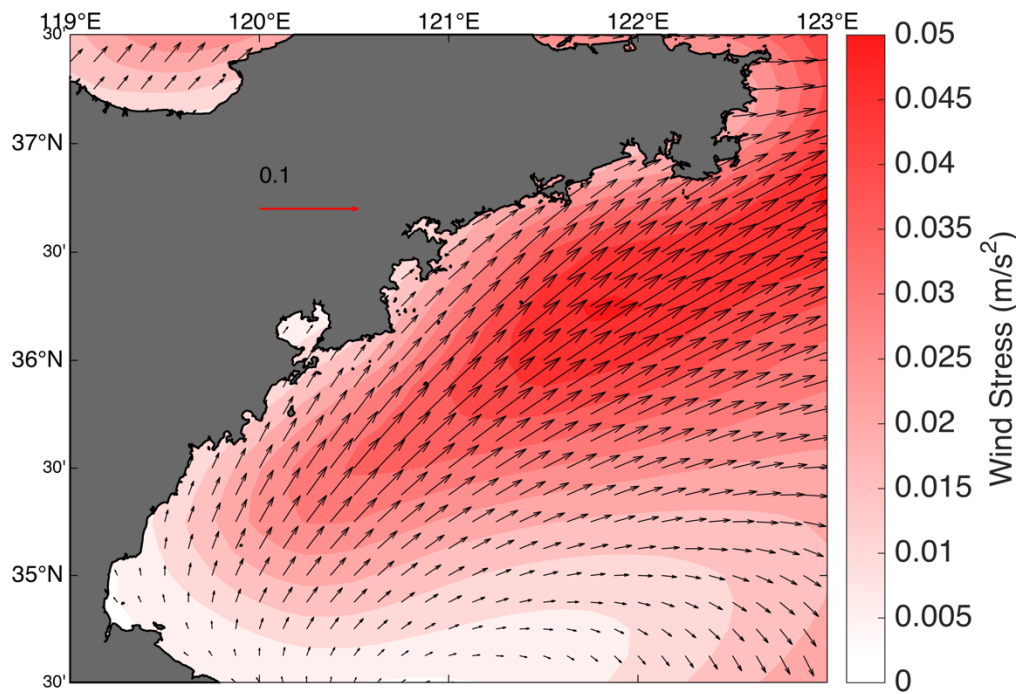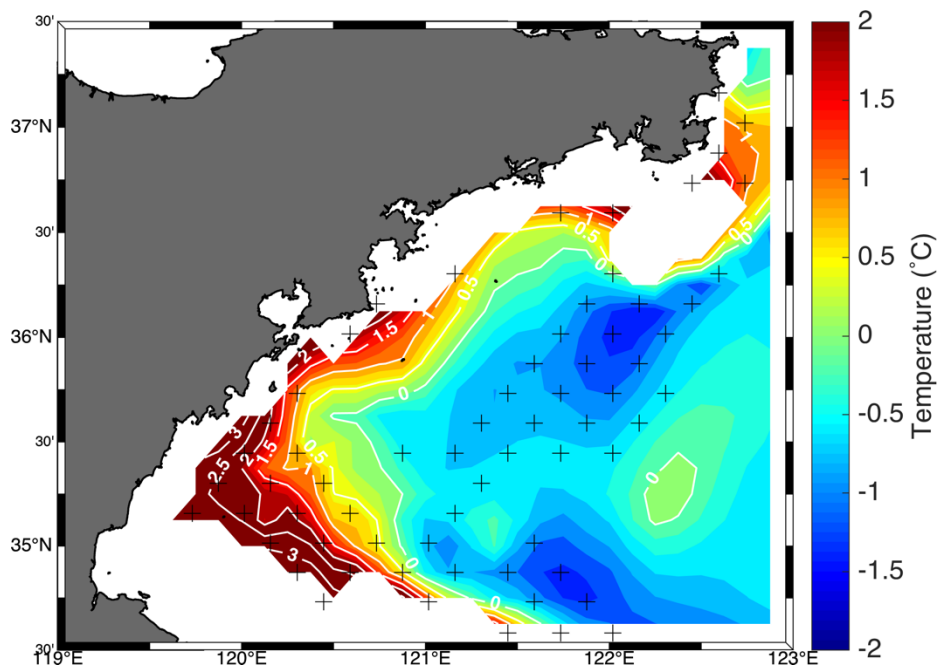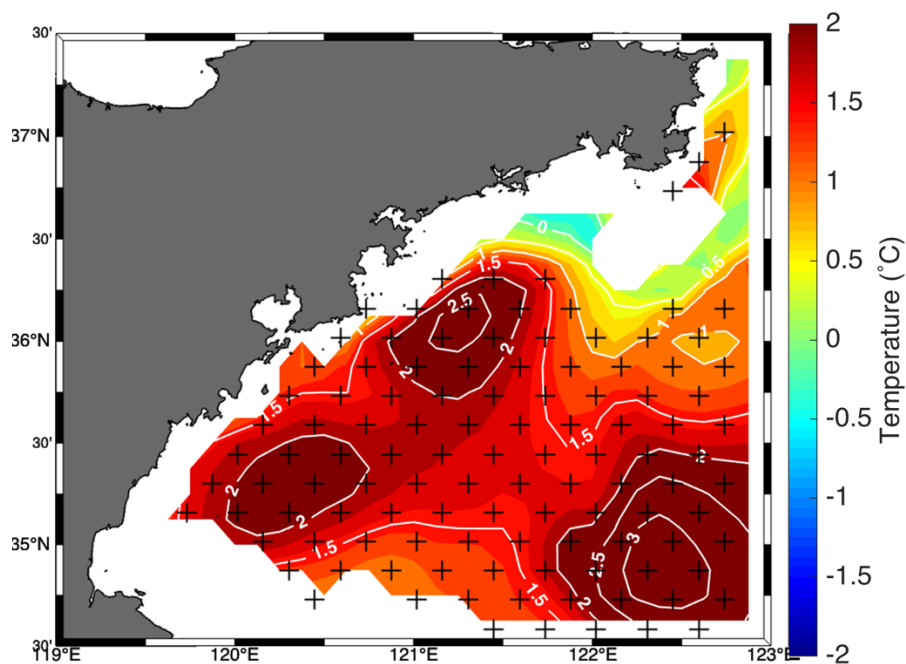
475

480 **Appendix**

Figure A1. The surface wind stress of the control run.

485

Figure A2. The difference in temperature between the control run and the run without tidal forcing. The crosses represent the areas where the difference between the control run and the run without tidal forcing was significant.

490

Figure A3. The difference in temperature between the control run and the run without wind forcings. The crosses represent the areas where the difference between the control run and the run without tidal forcing was significant.